PHYSICAL REVIEW E **108**, 035301 (2023)

Representative deflection angle for the single-deflection method of direct simulation Monte Carlo

Young Gie Ohr (오영기)[*]
Paichai University, Daejeon 35345, Republic of Korea

(Received 20 March 2023; accepted 7 August 2023; published 6 September 2023)

The total cross section of binary collision is, in general, unbounded due to the long-range interations of molecules. It is conventional to truncate the small angle deflections of collisions. The present work suggests an alternative way of avoiding the difficulty of unboundedness. We employ the mean value theorem of definite integral over the deflection angle for the cross section. A series of numerical experiments were carried out to look for the representative collision cross section through which the single-angle simulation is amenable to the solution of the Boltzmann equation. Results show that the cross section should be $\langle\Sigma\rangle = \Sigma_D^2/(2\Sigma_D - \Sigma_\mu)$, and the representative deflection for the single-angle simulation be $\cos\langle\chi\rangle = \Sigma_\mu/\Sigma_D - 1$, where Σ_D is the diffusion cross section and Σ_μ is the viscosity cross section. The single-angle computations for the inverse power law and the Lennard-Jones force law perfectly reproduce the conventional scattering algorithms for one-dimensional (1D) simulations of transport coefficients and 1D shock thickness. The computation costs for Lennard-Jones molecules are comparable to the costs for inverse power-law models.

DOI: 10.1103/PhysRevE.108.035301

I. INTRODUCTION

It is well known that the direct simulation Monte Carlo (DSMC) method provides a powerful numerical tool for simulating dilute gas flows in various nonequilibrium problems. The method has been well established through the pioneering efforts of Bird [1,2]. One of the most important aspects of the simulation may be estimating the collision probability between a pair of molecules selected within a volume element. The no-time counter (NTC) theory developed by Bird and further refined for two-dimensional (2D) and 3D problems [3,4] is an efficient and precise method for calculating this probability. Over the past several decades, many other collision counting methods have been proposed [5–7]. All these methods use the total collision cross section rather than the differential cross section to achieve their purpose.

DSMC is based on the assumption that the free flight of molecules can be decoupled from collisional events by considering binary. collisions. In this assumption, the directions of encountering and departing molecules in a collision are independent of the probability that the collision will actually occur. Postcollision velocities are estimated by assuming an isotropic scattering law [the variable hard sphere (VHS) model] or its variant [the variable soft sphere (VSS) model]. There seems to be no place for the differential cross section to play a role in the simulation, although the laws of mechanics rigorously predict postcollision deflections in terms of the trajectory equation of colliding molecules [8].

The total cross section is generally an unbounded, diverging quantity for both mathematical and physical reasons. A conventional way to avoid this unboundedness in DSMC is to cut off small deflections. Bird employed the other method [1]: His total cross section is exactly equal to $\frac{3}{2}$ times the viscosity cross section.

In the present paper, we suggest another way to avoid the unboundedness difficulty, introducing a "representative cross section" (RCS). Since the total cross section is an angle integration of the differential cross section over deflections, it can be expressed using the first mean value theorem for definite integrals [9] and by multiplying and dividing by an appropriate function,

$$\Sigma_t = 2\pi \int_0^\pi \Sigma_\chi \sin\chi \, d\chi, \tag{1a}$$

$$\langle\Sigma\rangle = \frac{2\pi}{F(\chi_0)} \int_0^\pi F(\chi)\Sigma_\chi \sin\chi \, d\chi, \tag{1b}$$

where Σ_t is the total cross section, Σ_χ is the differential cross section, $\langle\Sigma\rangle$ is the RCS, χ is the deflection angle, $F(\chi)$ is the appropriate integrable function, and χ_0 is a certain deflection angle within $0 < \chi_0 < \pi$. Equation (1b) suggests a cross section giving the deflection χ_0 for the postcollision velocities, leading us into a single-angle deflection simulation. The energy dependence of Σ_χ is reflected on the RCS through the trajectory equation for binary collisions.

The $F(\chi)$ is to be determined by numerical experiments for different χ_0's in the form of

$$F(\chi) = 1 - \cos^\ell \chi, \tag{2}$$

where ℓ is a positive integer. For $\ell = 1$ and 2, it gives the diffusion cross section (Σ_D) and the viscosity cross section (Σ_μ) [1], respectively,

$$\Sigma_D = 2\pi \int_0^\pi (1 - \cos\chi)\Sigma_\chi \sin\chi \, d\chi, \tag{3a}$$

$$\Sigma_\mu = 2\pi \int_0^\pi (1 - \cos^2\chi)\Sigma_\chi \sin\chi \, d\chi. \tag{3b}$$

---

[*] ohr@pcu.ac.kr

2470-0045/2023/108(3)/035301(16)

These are bounded integrals in contrast to the unbounded total cross section, Σ_t, in Eq. (1a).

In the conventional DSMC algorithm, deflection angles for postcollision velocities are estimated by randomly selecting impact parameters (actually, squares of them, representing an impact area). In the center-of-mass frame of reference, the uniformity of the impact area results in isotropic deflections of outgoing molecules. Any directionalities of nonequilibrium flows are reflected by the direction of the center-of-mass velocity according to the corresponding boundary condition, not by the direction of relative velocity. There is a report that more sophisticated scattering models for deflections cannot predict flow physics more representatively [10].

Since the deflection angle is one of the degrees of freedom in constructing the ensemble, its effect should be averaged at the end of the simulation. In this respect, the single-angle simulation can be regarded as a simulation using preaveraged deflections over uniform impact areas. This new algorithm not only saves one call to a random number generator but also reduces one degree of freedom in the ensemble generation. Successful simulation using a single angle implies that the effect of preaveraging over the impact area should have a small or negligible influence on the independence of the generated ensemble constituents.

The new algorithm is particularly useful for simulations of more realistic force models in which the attractive force is important, such as Lennard-Jones (L-J) molecules at low temperatures. Although Bird commented that "…it should not be assumed that an increase in physical realism necessarily leads to improved validation against experimental observation" [11], many efforts have been made to implement attractive intermolecular forces in DSMC [12–16], not only for physical realism but also for better understanding the nature of observations. However, computation tasks increase drastically when the attractive part is introduced to the binary collision event. The present study demonstrates that the single-angle computation of DSMC works well for attractive molecules with comparable costs to conventional inverse power law (IPL) molecules, which constitutes one of the most remarkable results.

Since the hard sphere (HS) is an archetypal model for DSMC, we first examine the RCS of HS by computing the mass, momentum, and energy transport coefficients. Then we apply the information obtained from HS to Maxwell molecules and L-J molecules and determine χ_0 and $F(\chi)$ in Sec. II. In Sec. III, we compare the results of single-angle simulations to theoretical predictions and measured values, along with the results of conventional computations. We also present an application to shock waves in the same section and discuss the coarser graining of fine meshed values and their statistical fluctuaton. We discuss some aspects of computation costs at the end of Sec. III and give concluding remarks in Sec. IV. A brief description of the collision dynamics of L-J molecules is provided in the Appendix, where the dynamics are analyzed into two branches: the repulsive and attractive branches. The limiting laws of strong and weak energy collisions are considered, and the results of numerical integrations for χ_0, $\langle\Sigma\rangle$, Σ_D, and Σ_μ are tabulated and presented in the Supplemental Material [17].

II. NUMERICAL EXPERIMENTS

The one-dimensional flows of dilute gases can be simulated with the use of Bird's 94-version of the DSMC program [1], DSMC1.FOR, which is the only version for which the FORTRAN source is available in the public domain. The program uses many initial parameters. Some of them are taken as fixed values throughout the present work, according to the following rules:

(i) The mean free path and the mean free flight time of HS are taken as $\lambda_H = 1/(\sqrt{2}\pi n d_H^2)$ and $\tau_H = \lambda_H/\sqrt{8k_B T_{\text{ref}}/(\pi m)}$, respectively, where d_H is the hard sphere diameter, n is the number density, and T_{ref} is a reference temperature.

(ii) The uniform cell width is equal to $0.1\lambda_H$, and each cell has 10 subcells.

(iii) The uniform time steps are equal to $0.01\tau_H$.

(iv) The time steps between samplings are eight steps ($\texttt{NIS} = 8$).

(v) There are 120 simulators in a cell.

Additional rules for transport coefficients: The distance between two boundaries is set $30\lambda_H$, and the number density (`FND`) is taken as 10^{20} m^{-3}. These rules give the number of cells, $\texttt{MNC} = 300$, the number of real molecules represented by one simulator, $\texttt{FNUM} = 2.78 \times 10^{15}$, and the number of simulators residing in a subcell is 1.2 in average. The maximum number of simulator is taken as $\texttt{MNM} = 2 \times 10^5$. For the computation of shock waves, a little different rule is to be applied. The steady state is assumed to be attained by 8×10^5 time steps, and the final results are taken by $\sim 8 \times 10^5$–8×10^7 time steps after the steady state.

The HS parameters are the standard VHS parameters of Ar, $m = 6.63 \times 10^{-26}$ kg, $d_H = 4.17 \times 10^{-10}$ m, and $T_{\text{ref}} = 273$ K, which are given in Bird's book [1].

The DSMC1.FOR uses the total cross section in FORTRAN variable `CVR` in the `SUBROUTINE SELECT`,

$$\texttt{CVR} = g\Sigma_t, \tag{4}$$

where g is the absolute value of the relative velocity of colliding molecules. In VHS theory, $\Sigma_t = \frac{3}{2}\Sigma_\mu$, which is reflected in the DSMC1.FOR. For the single-angle computations, the `CVR` is changed to

$$\texttt{CVR} = g\langle\Sigma\rangle. \tag{5}$$

The collision probability in NTC theory [1] depends on the value $g\Sigma_t/(g\Sigma_t)_{\text{max}}$. It is replaced by the change of `CVR` as

$$\frac{g\langle\Sigma\rangle}{(g\Sigma_t)_{\text{max}}}, \tag{6}$$

in which the denominator $(g\Sigma_t)_{\text{max}}$ is a number determined internally for each cell during the computation and given its initial value in the `SUBROUTINE INIT1` by the variable `CCG(1,M,L,K)`,

$$\texttt{CCG(1, M, L, K)} = \pi d_{\text{ref}}^2\sqrt{300T}, \tag{7}$$

where d_{ref} is a VHS parameter ($d_{\text{ref}} = d_H$ for HS) and T is the gas temperature. This number determines the value of the `COLLISION EVENT RATIO`, which is put into the generated file `DSMC1.OUT`. In conventional HS simulations, the event ratio is about 0.3. For simulations other than HS, there are occasions when the event ratio becomes abnormally close to 1. Therefore, we have introduced an adjustable parameter X to `CCG(1, M, L, K)`,

$$\mathtt{CCG(1,M,L,K)} = X\pi d_{\mathrm{ref}}^2\sqrt{300T}, \tag{8}$$

to make the event ratio about 0.3–0.5. For HS, $X = 1$; for Maxwell molecules, X has been assigned to the range 1–10 for final answers. The `COLLISION EVENT RATIO` is sensitive to X, but the final results of simulation is insensitive, although not independent of the event ratio.

The DSMC1.FOR provides an option for the selection of VSS computation by the formula,

$$\cos\chi = 2(R_f)^{\frac{1}{\alpha}} - 1, \tag{9}$$

in the `SUBROUTINE ELASTIC`, with an input of $1/\alpha$, where R_f designates the random number between 0 and 1. If one changes this formula by

$$\cos\chi = \cos\chi_0, \tag{10}$$

and gives an input for $\cos\chi_0$, then the program carries out the single deflection angle computation. Numerical experiments are performed for different $\cos\chi_0$'s.

It may be the right time to emphasize the fact that any spatial changes of physical properties are not so meaningful within a mean free path when the local Knudsen number is small (Kn < 0.1). The reason for using a cell width of $0.1\lambda_H$ and time steps as small as $0.01\tau_H$ is not to evaluate any properties with such precision but to reduce possible errors arising from the basic assumption of DSMC: the uncoupling of the free flight and collision event of simulators. Therefore, it is desirable to postprocess the simulated fine values by spatially coarser graining. We discuss this point in more detail in Sec. III D.

A. Hard spheres

By applying the above-mentioned changes to the FORTRAN program DSMC1.FOR, we conduct experiments for transport coefficients of HS using single deflection simulations. Results are compared to the theoretical values given by the Chapman-Enskog theory for the Boltzmann equation, which are

$$D_{11,\mathrm{CE}} = \frac{3}{8nd_H^2}\sqrt{\frac{k_BT}{\pi m}}(1+0.019), \tag{11a}$$

$$\mu_{\mathrm{CE}} = \frac{5m}{16d_H^2}\sqrt{\frac{k_BT}{\pi m}}(1+0.016), \tag{11b}$$

$$\kappa_{\mathrm{CE}} = \frac{75k_B}{64d_H^2}\sqrt{\frac{k_BT}{\pi m}}(1+0.025), \tag{11c}$$

the self-diffusion coefficient, the shear viscosity, and the thermal conductivity, respectively, where the decimal numbers in parentheses are the higher-order corrections in the Sonine polynomial expansions [18].

The differential cross section of HS, $\Sigma_\chi = \frac{1}{4}d_H^2$, gives

$$\Sigma_D = \pi d_H^2, \tag{12a}$$

$$\Sigma_\mu = \frac{2}{3}\pi d_H^2. \tag{12b}$$

The RCS in Eq. (1b) for HS, therefore, is given by

$$\langle\Sigma\rangle = \frac{\pi d_H^2}{1-\cos^\ell\chi_0}, \tag{13a}$$

for odd ℓ and

$$\langle\Sigma\rangle = \frac{\ell}{1+\ell}\frac{\pi d_H^2}{1-\cos^\ell\chi_0}, \tag{13b}$$

for even ℓ. The numerical experiments for HS determine the value of ℓ by the single-angle simulation for different deflections, $\cos\chi_0$, from −0.9 to 0.9.

1. Self-diffusion coefficients

Self-diffusion is a simple mass transport phenomenon of fluids through which molecular collisions in equilibrium can be studied. The DSMC1.FOR program simulates the binary mixture of two mechanically identical but distinguishable species by labeling each one and applying the stream boundary condition, `IB(1) = IB(2) = 4` at `XB(1)` and `XB(2)`, to a stationary gas with no stream velocity at the boundary, `BVFX(1) = BVFX(2) = 0`. The composition at each boundary is set to be pure of the two species, `BFSP(1, 1) = BFSP(2, 2) = 1`, `BFSP(1, 2) = BFSP(2, 1) = 0`, and `IIS = 1`. Following the method given in Bird's book [1], the results of simulation for HS at $T = 273$ K are shown in Fig. 1(a).

Figure 1(a) shows the ratio of the simulated self-diffusion coefficients to the theoretical values in Eq. (11a) versus $\cos\chi_0$ for $\ell = 1$, 2, and 3. The curves for $\ell \geqslant 4$ are too irrelevant and not drawn. The most important finding in this experiment is the perfect coincidence of the simulated values for $\ell = 1$ with the theory for all $\cos\chi_0$'s. The RCS in Eq. (1b) takes the form

$$\langle\Sigma\rangle = \frac{\Sigma_D}{1-\cos\chi_0}, \tag{14}$$

for any $0 < \chi_0 < \pi$ in the mass transports. It is noteworthy to observe that the curves for $\ell = 2$ and 3 cross the horizontal line, giving agreements with theory at the particular $\cos\chi_0$'s.

2. Shear viscosity

The DSMC1.FOR manifests the collisional momentum transfer through the shear viscosity of plane Couette flows. The solid boundaries are set by `IB(1) = IB(2) = 3` and `IIS = 2`, together with the velocity difference of 0.5Ma where $\mathrm{Ma} = \sqrt{5k_BT/(3m)}$, i.e., `BVY(1) = 0.25Ma`, `BVY(2) = −0.25Ma`; `BT(1) = BT(2) =` $T = 273$ K for equal wall temperatures.

Figure 1(b) shows the ratio of the simulated shear viscosities to the theoretical values in Eq. (11b) versus $\cos\chi_0$ for $\ell = 1$, 2, and 3. Due to viscous heating, the temperature around the center between the two moving walls is increased to about 277 K.

It is remarkable to observe that Fig. 1(b) shows that the simulated viscosities for $\ell = 2$ perfectly coincide with the theory for all $\cos\chi_0$'s, whereas the simulated diffusivities for $\ell = 1$ have shown the same behavior in Fig. 1(a). The RCS of momentum transports is therefore regarded as

$$\langle\Sigma\rangle = \frac{\Sigma_\mu}{1-\cos^2\chi_0}. \tag{15}$$

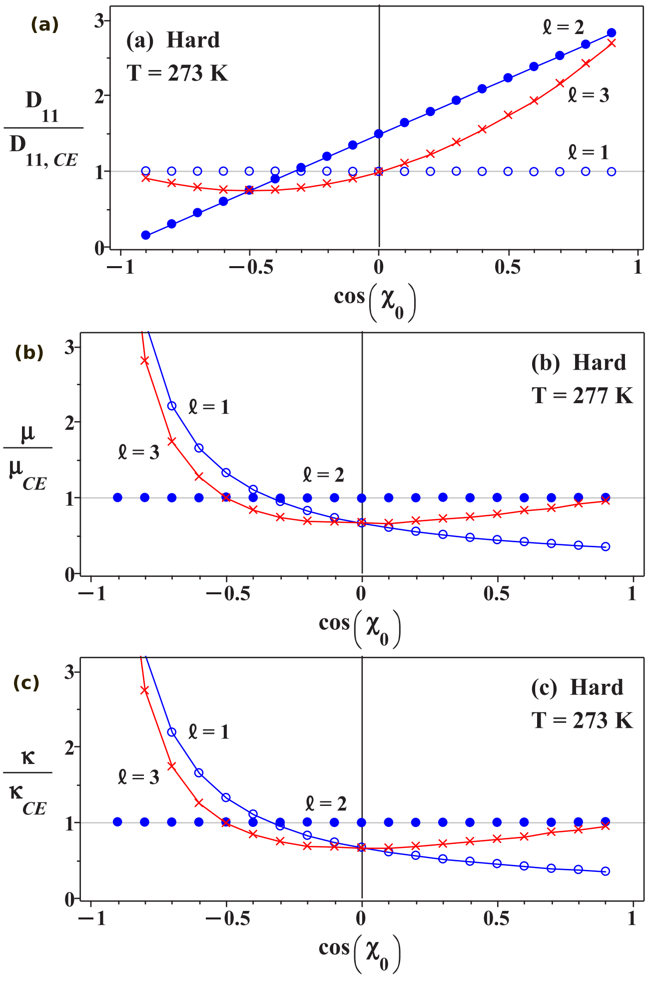

FIG. 1. Results of numerical experiments for hard spheres at the wall temperature of 273 K are shown. The temperatures designated in the figures are fluid temperatures. Empty circles represent $\ell = 1$, solid circles represent $\ell = 2$, and × symbols represent $\ell = 3$, of Eqs. (13). The upper figure (a) shows the results of self-diffusion coefficients as the ratio of the single-angle simulation to the theoretical values for the full range of deflections. The middle figure (b) displays the results of shear viscosity, and the bottom figure (c) shows those of thermal conductivity.

The curve for $\ell = 1$ in Fig. 1(b) crosses the horizontal line at almost the same point as the curve for $\ell = 2$ does in Fig. 1(a). The curves for $\ell = 3$ also cross the horizontal lines in both Figs. 1(a) and 1(b), but the crossing points are apparently different. Therefore, it is certain that both RCS in Eqs. (14) and (15) for $\ell = 1$ and 2 must be simultaneously true for both the simulated viscosities and diffusivities to be consistent with theoretical values,

$$\langle\Sigma\rangle = \frac{\Sigma_D}{1-\cos\chi_0} = \frac{\Sigma_\mu}{1-\cos^2\chi_0}, \tag{16}$$

which gives

$$\cos\chi_0 = \frac{\Sigma_\mu}{\Sigma_D} - 1 \tag{17}$$

and

$$\langle\Sigma\rangle = \frac{\Sigma_D^2}{2\Sigma_D - \Sigma_\mu}. \tag{18}$$

Equation (17) defines the "representative deflection angle" (RDA), writing $\langle\chi\rangle$,

$$\cos\langle\chi\rangle = \frac{\Sigma_\mu}{\Sigma_D} - 1. \tag{19}$$

Equation (18) is the definition of the RCS, which should always be positive since

$$\begin{aligned}2\Sigma_D - \Sigma_\mu &\sim \int [2(1-\cos\chi) - (1-\cos^2)]\Sigma_\chi \sin\chi\, d\chi \\ &= \int (1-\cos\chi)^2 \Sigma_\chi \sin\chi\, d\chi > 0 \end{aligned} \tag{20}$$

for $0 < \chi < \pi$. For hard spheres,

$$\cos\langle\chi\rangle = -\tfrac{1}{3} \ \text{ and } \langle\Sigma\rangle = \tfrac{3}{4}\pi d_H^2. \tag{21}$$

One may observe that the curve for $\ell = 2$ in Fig. 1(a) and the curve for $\ell = 1$ Fig. 1(b) cross horizontal lines at about $\cos\chi_0 = -\frac{1}{3}$ which is consistent with the obtained value.

3. *Thermal conductivity*

The collisional energy transfer of molecules in fluids is exhibited by thermal conductivity. The solid surface boundary condition is `IB(1)` = `IB(2)` = 3 and `IIS` = 2, with stationary boundaries `BVY(1)` = `BVY(2)` = 0 of different temperature: `BT(1)` = $T + 0.5\Delta T$ and `BT(2)` = $T - 0.5\Delta T$, where ΔT is taken as $0.3T$ and $T = 273$ K.

The simulation results are shown in Fig. 1(c). The figure almost duplicates the viscosity simulation in Fig. 1(b), which means that DSMC1.FOR reproduces Eucken's formula well [18],

$$\frac{\kappa}{\mu} = \frac{5}{2}c_v = \frac{15}{4}\frac{k_B}{m}. \tag{22}$$

B. Maxwell molecules

The intermolecular force of the IPL model takes the form $\Bbbk/r^\eta$ for $\eta > 1$, where $\Bbbk > 0$ is the repulsive force parameter and r is the intermolecular distance; $\eta = 5$ for Maxwell molecules. For a given η, the deflection angle of IPL molecules depends only on a single dimensionless parameter [1], defined by

$$z \equiv b\left(\frac{m_r g^2}{\Bbbk}\right)^{\frac{1}{\eta-1}}, \tag{23}$$

where b is the impact parameter of binary collisions and m_r is the reduced mass of two colliding molecules. According to Chapmann-Cowling [18], the viscosity of IPL molecules has the temperature dependence,

$$\mu \sim T^\omega, \tag{24}$$

where ω is given by

$$\omega = \frac{1}{2} + \frac{2}{\eta - 1}. \tag{25}$$

The force parameter $\Bbbk$ is determined by the measured viscosity at a certain reference temperature [1], writing μ_{ref} and T_{ref},

$$\frac{\Bbbk}{2k_B T_{\mathrm{ref}}} = \left[\frac{5}{8A_2}\frac{m}{\mu_{\mathrm{ref}}\Gamma\left(\frac{9}{2}-\omega\right)}\sqrt{\frac{k_B T_{\mathrm{ref}}}{\pi m}}\right]^{\frac{2}{2\omega-1}}, \tag{26}$$

in which Γ is the Gamma function and A_2 is defined below. The Σ_D and Σ_μ of IPL molecules are given in the forms

$$\Sigma_D = 2\pi A_1\left(\frac{\Bbbk}{m_r g^2}\right)^{\omega-\frac{1}{2}}, \tag{27a}$$

$$\Sigma_\mu = 2\pi A_2\left(\frac{\Bbbk}{m_r g^2}\right)^{\omega-\frac{1}{2}}, \tag{27b}$$

where A_1 and A_2 are pure numbers depending on ω only (coming in through the η dependence in z), defined by

$$A_1 = \int_0^\infty (1-\cos\chi)z\,dz, \tag{28a}$$

$$A_2 = \int_0^\infty (1-\cos^2\chi)z\,dz. \tag{28b}$$

The A_1 and A_2 are tabulated in the literature by Koura and Matsumoto [12]. Therefore, Σ_D and Σ_μ are estimated by the literature values for A_1, A_2, and μ_{ref} measured at T_{ref}. Substituting Eq. (26) into Eqs. (27),

$$\Sigma_D = \frac{2A_1}{3A_2}\Sigma_{\mathrm{VHS}}, \tag{29a}$$

$$\Sigma_\mu = \frac{2}{3}\Sigma_{\mathrm{VHS}}, \tag{29b}$$

where

$$\Sigma_{\mathrm{VHS}} = \frac{15}{8}\frac{\sqrt{\pi m k_B T_{\mathrm{ref}}}}{\mu_{\mathrm{ref}}\Gamma\left(\frac{9}{2}-\omega\right)}\left(\frac{2k_B T_{\mathrm{ref}}}{m_r g^2}\right)^{\omega-\frac{1}{2}}. \tag{30}$$

It is conventional to write the Σ_{VHS} in terms of the reference diameter, d_{ref}, defined by

$$\pi d_{\mathrm{ref}}^2 = \frac{15\sqrt{\pi m k_B T_{\mathrm{ref}}}}{2\mu_{\mathrm{ref}}(7-2\omega)(5-2\omega)}. \tag{31}$$

Then, we have

$$\Sigma_{\mathrm{VHS}} = \frac{\pi d_{\mathrm{ref}}^2}{\Gamma\left(\frac{5}{2}-\omega\right)}\left(\frac{2k_B T_{\mathrm{ref}}}{m_r g^2}\right)^{\omega-\frac{1}{2}}. \tag{32}$$

The Σ_{VHS} in Eq. (32) is the total cross section in Bird's VHS theory, used to define the FORTRAN variable `CVR` in the DSMC1.FOR as mentioned in Eq. (4).

Since the experiment with $\ell = 1$ utilizes the Σ_D in Eq. (29a), we need A_1 and A_2 for Maxwell molecules [12],

$$A_1 = 0.4219, \quad A_2 = 0.4362. \tag{33}$$

The theoretical transport coefficients are given by the Chapman-Enskog solutions for the Boltzmann equation, which can be written in our current notations as

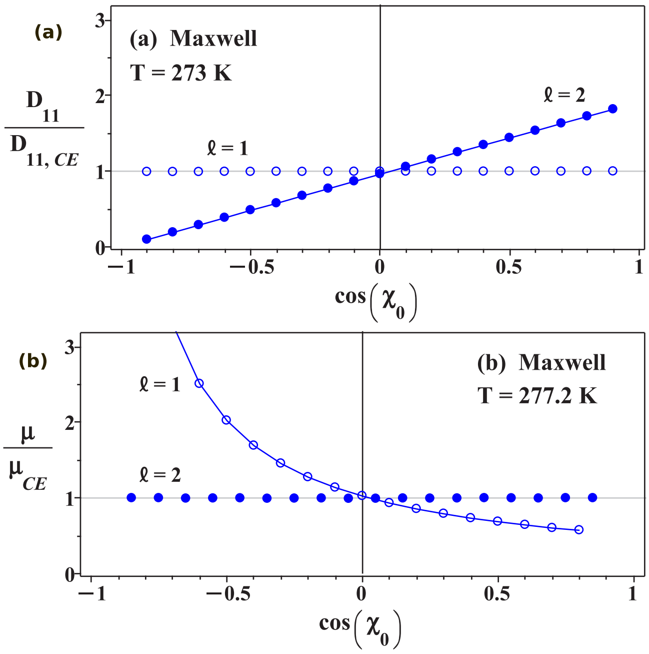

FIG. 2. Results of numerical experiments for Maxwell molecules at the wall temperature of 273 K are shown. The temperatures designated in the figures are fluid temperatures. Empty circles represent $\ell = 1$, and solid circles represent $\ell = 2$. The upper figure (a) shows the results of self-diffusion coefficients by the ratio of the single-angle simulation to the theoretical values for the full range of deflections. The lower figure (b) displays the results of shear viscosity.

$$D_{11,\mathrm{CE}} = \frac{3(7-2\omega)}{10nm}\frac{A_2}{A_1}\mu_{\mathrm{CE}}, \tag{34a}$$

$$\mu_{\mathrm{CE}} = \mu_{\mathrm{ref}}\left(\frac{T}{T_{\mathrm{ref}}}\right)^\omega = \frac{15m}{2d_{\mathrm{ref}}^2}\frac{(T/T_{\mathrm{ref}})^\omega}{(7-2\omega)(5-2\omega)}\sqrt{\frac{k_B T_{\mathrm{ref}}}{\pi m}}, \tag{34b}$$

$$\kappa_{\mathrm{CE}} = \frac{15k_B}{4m}\mu_{\mathrm{CE}}, \tag{34c}$$

where $\omega = 1$ for Maxwell molecules.

Numerical experiments are carried out by the use of RCS in Eq. (1b) and cross sections in Eqs. (29),

$$\langle\Sigma\rangle = \frac{1}{1-\cos^\ell\chi_0}\Sigma_\ell, \tag{35}$$

where $\Sigma_1 \equiv \Sigma_D$ and $\Sigma_2 \equiv \Sigma_\mu$ for $\ell = 1$ and 2, respectively. Figure 2 shows the results of experiments. Because the experiments on thermal conductivity show almost equivalent behaviors to viscosity, we have not drawn duplicate figures. As shown in the figure, the experiments for Maxwell molecules show exactly the same behaviors of transport coefficients as those of HS, except for the location of the crossing point on the horizontal line. Substituting Eqs. (29) into (18) and (19), we obtain

$$\langle\Sigma\rangle = \frac{\Sigma_D^2}{2\Sigma_D - \Sigma_\mu} = \frac{\Sigma_D}{2 - A_2/A_1} \equiv \xi^2\Sigma_{\mathrm{VHS}} \tag{36}$$

and

$$\cos\langle\chi\rangle = \frac{\Sigma_\mu}{\Sigma_D} - 1 = \frac{A_2}{A_1} - 1, \tag{37}$$

where

$$\xi^2 \equiv \frac{2A_1^2}{3A_2(2A_1 - A_2)}. \tag{38}$$

The ξ^2 in Eq. (36) is a scaling parameter which is equal to $\frac{3}{4}$ for HS [Eq. (21)], and

$$\xi^2 = 0.6674, \quad \cos\langle\chi\rangle = 0.0339, \tag{39}$$

for Maxwell molecules. One can confirm again that the curve for $\ell = 2$ in Fig. 2(a) and the curve for $\ell = 1$ in Fig. 2(b) cross the horizontal lines at $\cos\chi_0 = 0.0339$ predicted in Eq. (39).

C. Lennard-Jones molecules

The L-J potential is written in the form

$$V = 4\epsilon\left[\left(\frac{\sigma}{r}\right)^{12} - \left(\frac{\sigma}{r}\right)^{6}\right], \tag{40}$$

with the potential minimum, ϵ, and the contact distance, σ. The dynamics of binary collision of L-J molecules have been well studied in the literature [19]. What we need for experiments are Σ_D and Σ_μ. In dimensionless forms,

$$\widetilde{\Sigma}_D = \int_0^\infty (1 - \cos\chi)\widetilde{b}d\widetilde{b}, \tag{41a}$$

$$\widetilde{\Sigma}_\mu = \int_0^\infty (1 - \cos^2\chi)\widetilde{b}d\widetilde{b}, \tag{41b}$$

where

$$\widetilde{\Sigma}_D \equiv \frac{\Sigma_D}{2\pi\sigma^2}, \quad \widetilde{\Sigma}_\mu \equiv \frac{\Sigma_\mu}{2\pi\sigma^2}, \quad \widetilde{b} \equiv \frac{b}{\sigma}. \tag{42}$$

One more parameter for the experiment is the reference diameter of colliding molecules, which corresponds to d_{ref} of VHS computations and is used for $(g\Sigma_t)_{\text{max}}$ of the NTC theory in Eq. (8). It is reasonable to take it as the distance at which the L-J potential is equal to 0, writing

$$(g\Sigma_t)_{\text{max}} = X\pi\sigma^2\sqrt{300T}, \tag{43}$$

for the initial number. Then the $(g\Sigma_t)_{\text{max}}$ value is adjusted by the parameter $X = 1$–15 in order to have the `COLLISION EVEN RATIO` in the range 0.3–0.5.

The theoretical transport coefficients of L-J molecules take the forms [19]

$$D_{11,\text{CE}} = \frac{3}{8n\sigma^2}\frac{1}{\Omega^{(1,1)*}}\sqrt{\frac{k_BT}{\pi m}}, \tag{44a}$$

$$\mu_{\text{CE}} = \frac{5m}{16\sigma^2}\frac{1}{\Omega^{(2,2)*}}\sqrt{\frac{k_BT}{\pi m}}, \tag{44b}$$

$$\kappa_{\text{CE}} = \frac{15k_B}{4m}\mu_{\text{CE}}, \tag{44c}$$

where

$$\Omega^{(1,1)*} = \int_0^\infty \widetilde{\Sigma}_D x^2 e^{-x} dx, \tag{45a}$$

$$\Omega^{(2,2)*} = \frac{1}{2}\int_0^\infty \widetilde{\Sigma}_\mu x^3 e^{-x} dx, \tag{45b}$$

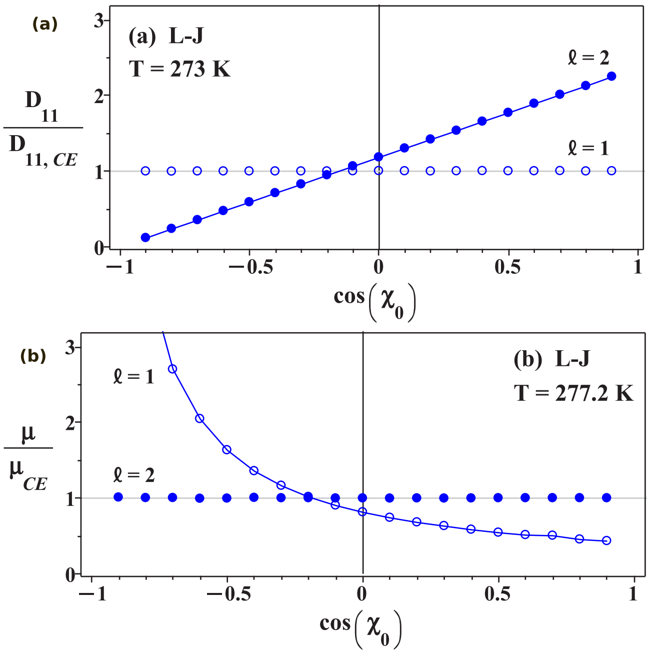

FIG. 3. Results of numerical experiments for Lennard-Jones molecules at the wall temperature of 273 K are shown. The temperatures designated in the figures are fluid temperatures. Empty circles represent $\ell = 1$, and solid circles represent $\ell = 2$. The upper figure (a) shows the results of self-diffusion coefficients as the ratio of the single angle simulation to theoretical values for the full range of deflections. The lower figure (b) displays the results of shear viscosity.

and

$$x \equiv \frac{m_r g^2}{2k_BT}. \tag{46}$$

The look-up tables for $\widetilde{\Sigma}_D$ and $\widetilde{\Sigma}_\mu$ are prepared in the present work and described in the Appendix.

The L-J parameters taken are the standard values for Ar [19], $\epsilon/k_B = 124$ K, and $\sigma = 3.418 \times 10^{-10}$ m. Results of experiments are shown in Fig. 3. As shown in the figure, the behaviors of transport coefficients for L-J molecules are again the same as those for HS and Maxwell molecules.

Apparently, the formulas for RCS and RDA in Eqs. (18) and (19) are also true for L-J molecules, which should be g-dependent values,

$$\langle\widetilde{\Sigma}\rangle = \frac{\widetilde{\Sigma}_D^2}{2\widetilde{\Sigma}_D - \widetilde{\Sigma}_\mu}, \quad \cos\langle\chi\rangle = \frac{\widetilde{\Sigma}_\mu}{\widetilde{\Sigma}_D} - 1, \tag{47}$$

where

$$\langle\widetilde{\Sigma}\rangle \equiv \frac{\langle\Sigma\rangle}{2\pi\sigma^2}. \tag{48}$$

The numerical values of $\langle\widetilde{\Sigma}\rangle$ and $\cos\langle\chi\rangle$ are tabulated in the Supplemental Material [17] and plotted in Figs. 4.

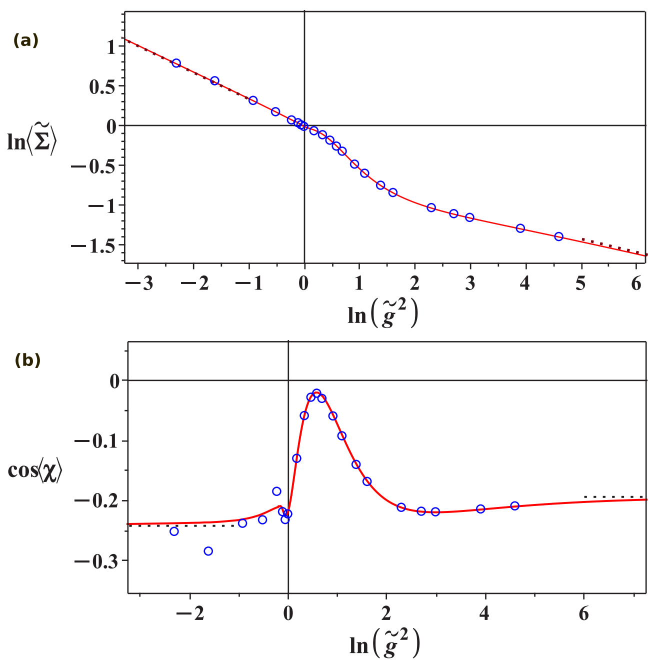

FIG. 4. Behaviors of the representative collision cross section in (a) and the representative deflection angle in (b) versus collisional energy in logarithm of dimensionless forms defined in Eqs. (48) and (A3) are shown. Circles represent the values computed using the literature values given by Hirschfelder, and dotted lines represent the limiting values given in Eqs. (A32c), (A32d), (A34c), and (A34d).

III. DISCUSSIONS

A. Comparison with theoretical values

The RCS and RDA are determined by the condition that the simulations of mass transport, momentum transport, and energy transport are simultaneously consistent with the theoretical values given by the Chapman-Enskog theory for the Boltzmann equation at a specific temperature. This consistency is also remarkable at other temperatures. For illustrative purposes, the computations for Maxwell molecules are shown in Table I. The fact that the simulations reproduce the theoretical values demonstrates that the simulation algorithm is appropriate for representing the solution of the Boltzmann equation.

It is well known that the conventional VHS method shows a deficiency in computing the diffusivity of IPL molecules (except for HS), while it accurately reproduces other transport coefficients [1,12], as shown in Table I. The VSS theory has been developed to overcome this defect by introducing a small extension to the scattering law and writing the impact parameter as follows:

$$b = d\cos^{\alpha}\left(\frac{\chi}{2}\right), \tag{49}$$

where d is an energy dependent collision diameter and α is a positive parameter which depends also on the colliding energy in general; $\alpha = 1$ for HS or VHS computations.

TABLE I. Temperature dependence of simulated transport coefficients of Maxwell molecules relative to the theoretical values given in Eqs. (34).

T (K)	Present	VHS	VSS
	$(D_{11}/D_{11,\text{CE}} - 1) \times 100$		
80	0.12	−36	−1.0
273	0.02	−36	0.02
640	−0.45	−36	−0.45
1500	−0.49	−36	−0.33
	$(\mu/\mu_{\text{CE}} - 1) \times 100$		
81.3	−1.4	−1.0	−1.0
277.3	−0.96	−0.89	−0.15
650.3	−0.80	−0.75	−0.42
1524.	−0.60	−0.68	−0.75
	$(\kappa/\kappa_{\text{CE}} - 1) \times 100$		
80	−0.83	−0.49	−0.49
273	−0.63	0.37	−0.63
640	−0.74	−0.53	−0.32
1500	−0.58	−0.40	−0.58

According to Koura and Matsumoto [12,20], the α and the total cross section (Σ_{VSS}) are given by Σ_D and Σ_μ,

$$\alpha = \frac{2\Sigma_\mu}{2\Sigma_D - \Sigma_\mu}, \tag{50a}$$

$$\Sigma_{\text{VSS}} = \frac{\Sigma_D}{2}\frac{2\Sigma_D + \Sigma_\mu}{2\Sigma_D - \Sigma_\mu}. \tag{50b}$$

The VSS theory can be applied to any force models as long as Σ_D and Σ_μ are given. For IPL molecules, Eqs. (29) give

$$\alpha = \frac{2A_2}{2A_1 - A_2}, \tag{51a}$$

$$\Sigma_{\text{VSS}} = \frac{(1+\alpha)(2+\alpha)}{6\alpha}\Sigma_{\text{VHS}}, \tag{51b}$$

which become $\alpha = 2.140$ and $\Sigma_{\text{VSS}} = 1.012\Sigma_{\text{VHS}}$ for Maxwell molecules by the A_1 and A_2 in Eq. (33). These values are used for the VSS computations given in Table I.

B. Comparison with measured values

As Bird mentioned [11], the main advantage of DSMC is its validity against experimental observations. It is demonstrated here that L-J computations are superior to the conventional IPL model in terms of validity, especially at low temperatures. All computations were carried out for Ar gas. The molecular force parameters are the most up-to-date values given by Weaver and Alexeenko in 2015 [15]: For the IPL model, $\omega = 0.697$, $\alpha = 1.311$, $d_{\text{ref}} = 3.5645 \times 10^{-10}$ m, $\mu_{\text{ref}} = 35.07 \times 10^{-6}$ Pa s, and $T_{\text{ref}} = 523.15$ K; for the L-J, $\epsilon/k_B = 143.78$ K and $\sigma = 3.3237 \times 10^{-10}$ m. The measured values taken for comparisons with computations are the reference values [21,22] which were used to determine the force parameters.

Caution is needed when using these parameters. In VHS theory, the reference diameter, denoted as $d_{\text{ref,VHS}}$ to avoid confusion, should be determined by the measured viscosity (μ_{ref}) and its temperature dependence (ω) at T_{ref} according to the formula in Eq. (31),

$$d_{\mathrm{ref,VHS}} = 3.614 \times 10^{-10}\ \mathrm{m}, \tag{52}$$

This value is different from that of Weaver and Alexeenko. For the VHS computations, the value of $d_{\mathrm{ref,VHS}}$ in Eq. (52) should be used together with $\alpha = 1$. Because the VHS method shows some discrepancies with experimental diffusivity results, the VSS method is conventionally used. When a value for ω is given, the VSS parameter α is determined. Since ω gives A_1 and A_2 in Eqs. (28) uniquely, the α is obtained by the use of Eq. (51a). For $\omega = 0.697$, they are

$$A_1 = 0.3837, \quad A_2 = 0.3181, \tag{53}$$

and

$$\alpha_{\mathrm{vss}} = 1.416, \tag{54}$$

in which the subscript "vss" of α is put to distinguish from the Weaver and Alexeenko's value, $\alpha = 1.311$. Weaver and Alexeenko have optimized the α by the best fitting of measured Schmidt numbers, and their d_{ref} is also the optimized value according to the formula in Eq. (51b), i.e.,

$$d_{\mathrm{ref}} = \sqrt{\frac{(1+\alpha)(2+\alpha)}{6\alpha}}\, d_{\mathrm{ref,VHS}}. \tag{55}$$

The unoptimized genuine value should be

$$\begin{aligned} d_{\mathrm{ref,VSS}} &= \sqrt{\frac{(1+\alpha_{\mathrm{vss}})(2+\alpha_{\mathrm{vss}})}{6\alpha_{\mathrm{vss}}}}\, d_{\mathrm{ref,VHS}} \\ &= 3.562 \times 10^{-10}\ \mathrm{m}. \end{aligned} \tag{56}$$

For comparison purposes, we carry out two VSS computations of the diffusivity of IPL molecules. One computation uses the values $d_{\mathrm{ref,VSS}}$ and α_{vss}, while the other uses the optimized values of Weaver and Alexeenko. These results are compared in Fig. 5(a).

For single-angle computations of the IPL model, we need the RDA and RCS values, which are given in Eqs. (36), (37), (38), and (53),

$$\langle \Sigma \rangle = \frac{2A_1^2}{3A_2(2A_1 - A_2)} \Sigma_{\mathrm{VHS}} = 0.6867 \Sigma_{\mathrm{VHS}}, \tag{57a}$$

$$\cos\langle \chi \rangle = \frac{A_2}{A_1} - 1 = -0.1710. \tag{57b}$$

The Σ_{VHS} in Eq. (57a) should be evaluated by Eqs. (32) and (52).

The L-J computations are also carried out in two ways. One is a single-angle computation using a look-up table for Σ_D and Σ_μ. The other is a VSS computation using formulas in Eqs. (9) and (50) and the same look-up table. It is interesting to compare the accuracy, which is shown in Figs. 5 using different symbols (solid circles for LJ-VSS and empty circles for the present work, denoted as LJ-RDA).

1. *Self-diffusion coefficient*

Let us first look at the diffusivity. Figure 5(a) shows the ratios of computed values to measured values [21] at some interpolated temperatures. The various symbols in the figure denote different computations: empty symbols represent single-angle computations and solid symbols represent conventional computations. The dotted lines along the symbols indicate the corresponding theoretical values in Eqs. (34a) and (44a).

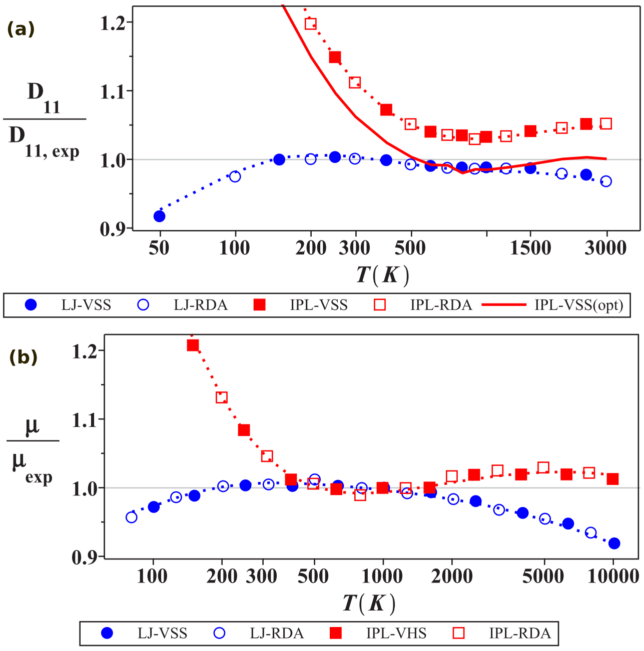

FIG. 5. Ratios of simulated self-diffusion coefficients in (a) and viscosity in (b), relative to their measured values, are shown. LJ-VSS represents VSS simulation of L-J molecules by using Eqs. (50) and the look-up table. LJ-RDA represents single-angle simulation of L-J molecules by using the same look-up table. IPL-VSS represents VSS simulations of IPL molecules by using parameters in Eqs. (54) and (56). IPL-RDA represents single-angle simulation of IPL molecules. IPL-VSS(opt) represents VSS simulation of IPL molecules by using the optimized parameters of Weaver and Alexeenko. Dotted lines along symbols represent the corresponding theoretical values in Eqs. (34a), (34b), (44a), and (44b).

For IPL molecules, the conventional VHS theory does not accurately represent diffusivity, as shown for Maxwell molecules in Table I. Therefore, we use the VSS method for conventional computations. The VSS computations are twofold: One computation follows Koura and Matsumoto's original method (represented by solid box symbols) using formulas in Eqs. (51), (53), and (56); the other computation uses the optimized parameters of Weaver and Alexeenko (represented by a thick solid line). As shown in the figure, the computation using optimized parameters shows good agreement with measured values at $T > 300$ K but has some discrepancies from theoretical values. On the other hand, both single-angle computations (represented by empty box symbols) and original VSS computations (represented by solid box symbols) closely reproduce theoretical values (represented by a dotted line), while showing some discrepancies from measured values.

For L-J molecules (represented by circular symbols), we carry out two types of computations: single-angle computations (represented by empty circles) and VSS computations (represented by solid circles). Both types of computations are consistent and perfectly reproduce theoretical values (represented by a dotted line). The L-J force model has an error of less than 1% relative to experimental values for $150\ \mathrm{K} < T < 1500\ \mathrm{K}$, which is much better than the IPL force model at temperatures below 400 K. The validity of L-J simulations against measurements seems superior to that of the IPL force model, especially at low temperatures.

2. *Shear viscosity*

Comparisons of simulated viscosities to measured values [22] are shown in Fig. 5(b) as ratios of simulated to measured values. For IPL molecules, VSS computations do not show any significant differences from VHS computations, regardless of whether optimized or unoptimized VSS parameters are used. Therefore, we use the VHS method for conventional simulations. Boxed symbols represent IPL molecules and circular symbols represent L-J molecules; empty symbols represent single-angle computations and solid symbols represent conventional computations. The dotted lines along the symbols indicate the corresponding theoretical values in formulas of Eqs. (34b) and (44b). It is apparent that all simulations accurately reproduce theoretical values. In terms of validity against measurements, the IPL force model works well for $T > 300$ K, while the L-J force model is again superior to the IPL at low temperatures

At very high temperatures ($T > 3000$ K), IPL computations are better than L-J computations. This may be due to the fact that the repulsive part of intermolecular forces is dominant in high-speed collisions and the rigidity of IPL, $\omega = 0.697$ [which corresponds to $\eta = 11.15$ in Eq. (25)], is more appropriate than the L-J (12-6) repulsion, $\eta = 13$.

3. *Shock wave thickness*

To further examine the single deflection angle simulation, 1D normal shock waves are computed using Bird's program, DSMC1S.FOR [1] . The computational procedures are the same as those of the 1D Couette program, DSMC1.FOR, except for some changes to initial parameters: The number of cells is increased to `MNC` = 500–1500 to set the distance between the upstream and downstream limits to be about 15 times the shock thickness, while keeping a cell width of $0.1\lambda_H$ and 10 subcells per cell. The maximum number of simulators is then increased to `MNM` $= 5 \times 10^5$–15×10^5.

In 1976, Alsmeyer measured the shock wave thickness of common gases and compared it with other observations [23]. Despite considerable experimental scatter, we have redrawn the reciprocal shock thickness of Ar in Fig. 6 and compared it with our computations. To follow the experimental conditions, we used Ar gas at $T = 300$ K and $p = 0.05$ torr, which corresponds to a number density of `FND` $= 1.61 \times 10^{21}$. We also used an upstream mean free path of 1.098×10^{-3} m, which Alsmeyer used to present shock profiles.

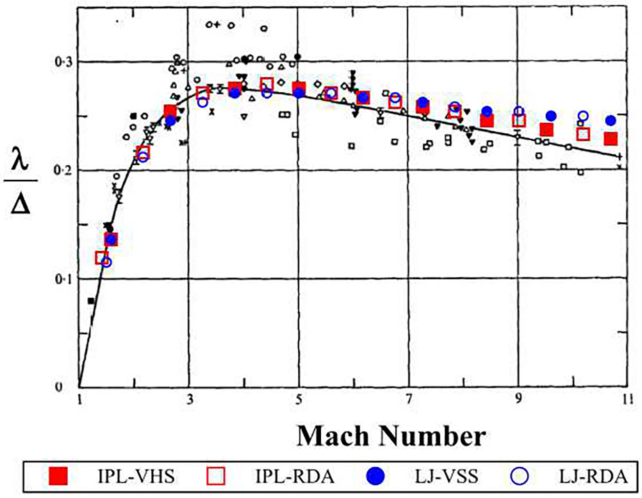

FIG. 6. The dimensionless inverse shock thickness, λ/Δ, of Argon vs Mach numbers is shown. Small scattered symbols represent measured values, and the solid line represents the compiled curve of them. Solid boxes represent VHS of IPL molecules. Empty boxes represent single-angle computation of IPL molecules. Solid circles represent VSS computations of L-J molecules using the look-up table. Empty circles represent single-angle computation of L-J molecules using the same look-up table.

In DSMC computations for shock waves, the outputs of density and flow rate are postprocessed. In principle, they should satisfy the continuity equation if the simulation is sufficiently accurate. Therefore, their numerical fluctuations should be smoothed by postprocessing. The continuity equation for shock waves demands

$$\rho u_x = \rho^{(u)} u_x^{(u)}, \tag{58}$$

where ρ and u_x are the density and the flow rate, respectively, and the superscripts (u)'s denote the upstream values. The simulated values should satisfy

$$\frac{\rho}{\rho^{(u)}} \frac{u_x}{u_x^{(u)}} = 1. \tag{59}$$

Because $\rho^{(u)}$ and $u_x^{(u)}$ are known values for the given Mach number, the postprocessing can be carried out by taking the arithmetic mean,

$$\widetilde{\rho} \equiv \frac{1}{2}\left[\left(\frac{\rho}{\rho^{(u)}}\right)_{\mathrm{DSMC}} + \left(\frac{u_x}{u_x^{(u)}}\right)^{-1}_{\mathrm{DSMC}}\right], \tag{60a}$$

$$\widetilde{u} \equiv \frac{1}{\widetilde{\rho}}. \tag{60b}$$

The coordinate origin is usually defined at the location of half-density,

$$\rho(0) = \tfrac{1}{2}[\rho^{(u)} + \rho^{(d)}], \tag{61}$$

where $\rho^{(d)}$ is the downstream density. After the postprocessing, the value of density is changed a little and gives

$$\rho'(\delta) = \tfrac{1}{2}[\rho^{(u)} + \rho^{(d)}], \tag{62}$$

where ρ' is the changed density by the postprocessing. Therefore, the coordinates should be translated, $x' = x - \delta$, in order to have

$$\widetilde{\rho}(0) = \tfrac{1}{2}[1 + \widetilde{\rho}^{(d)}], \tag{63}$$

where $\widetilde{\rho}^{(d)} = \rho^{(d)}/\rho^{(u)}$, the reduced downstream density. Then, all the $\widetilde{\rho}$ of different Mach numbers have common origin.

The reciprocal shock wave thickness is an important physical quantity of 1D shock waves, which represents the Knudsen number of shock waves. It can be defined by the maximum density slope,

$$\begin{aligned}\frac{\lambda}{\Delta} &= \frac{1}{\rho^{(d)}-\rho^{(u)}}\left[\frac{d\rho}{d\widetilde{x}}\right]_{\max}\\ &= \frac{1}{\widetilde{\rho}^{(d)}-1}\left[\frac{d\widetilde{\rho}}{d\widetilde{x}}\right]_{\max},\end{aligned} \tag{64}$$

where Δ is the shock thickness, λ is the mean free path of upstream molecules, and $\widetilde{x} = x/\lambda$, the reduced distance.

In shock wave simulations of IPL molecules, there are no significant differences between VHS and VSS computations. Results of computations are shown in Fig. 6. The solid line represents measured values compiled by Alsmeyer, circular symbols represent L-J computations, and boxed symbols represent IPL computations; empty symbols represent our computations and solid symbols represent conventional VHS (for IPL) and VSS (for L-J) computations. As shown in the figure, single-angle simulations perfectly reproduce conventional ones for both IPL and L-J force models. At very high Mach numbers, IPL computations are better than L-J computations. This may be due to the same reason that viscosity computations show at very high temperatures.

C. Collision frequency

It has been conventional to test the DSMC algorithm calculating the mean collision frequency in an equilibrium gas. The NTC algorithm is designed to cope with the test. The zero-dimensional single-cell code, DSMC0.FOR, one of the 94-family of old DSMC codes, can be used for this purpose. Because the collision number is determined by the total cross section at a certain density and temperature, regardless of the deflection laws, the RCS gives different collision frequencies from the theoretical values. For HS, $\langle\Sigma\rangle = \frac{3}{4}\pi d_H^2$, in Eq. (21), which gives the collision frequency exactly $\frac{3}{4}$ times the theoretical value. Let us recall that the single-angle algorithm reproduces the transport coefficients not only of the conventional but also of the theoretical predictions. This implies that one collision in the new algorithm represents $\frac{4}{3}$ collisions of actual HS collisions on average. This understanding is parallel to the postulate that one simulator represents the `FNUM` real molecules in Monte Carlo simulations. The lessened collision number in the single-angle simulation is regarded as a consequence of the reduction of one degree of freedom.

Since the DSMC program outputs the cumulative collision numbers for each restarting run, we can examine the total collision number (the FORTRAN variable `NCOL` in DSMC1C.FOR) as a function of time steps. Figure 7(a) shows this for different computations. The `NCOL`s are almost straight lines versus elapsed time steps. The slope gives the collision frequency,

$$\text{collision frequency} = \frac{d(\text{NCOL})}{d(\text{time step})}, \tag{65}$$

the values of which are shown in Table II.

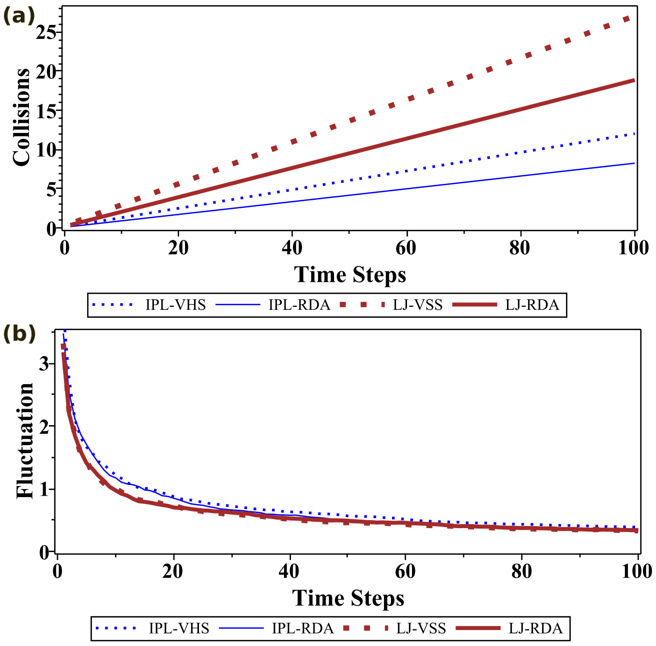

FIG. 7. These figures show the computaion for the *xy* component of the stress tensor of viscous flows: (a) The total collision number (`NCOL`) versus elapsed time steps; (b) the total fluctuation given in Eq. (70) versus time steps. The time steps are in increments of 8×10^3, the collision numbers are in 10^8, and the fluctuations are in arbitrary units.

D. Coarse graining

The coarser graining of simulated fine values is a successive moving average of the values accommodated in cells. It gives smoothed values averaged over a certain interval. Let Q_i be the simulated value at the ith cell, where $1 \leqslant i \leqslant \mathtt{MNC}$ and `MNC` is the total number of cells. The cell widths are assumed to be uniform. The $(2k+1)$ cells moving average is defined by

$$\bar{Q}_j \equiv \frac{1}{2k+1}\sum_{i=1}^{2k+1} Q_{j+i-1},\ j = 1,\ldots,\mathtt{MNC}-2k. \tag{66}$$

TABLE II. A crude estimation of collision frequencies and relative computing costs for the viscosities, diffusivities, and shock waves. (The relative values for diffusivity are relative to the IPL-VSS computations.) The ranges of computing costs are for the different machines used.

	IPL-VHS	IPL-RDA	LJ-VSS	LJ-RDA
		Viscosity (300 K)		
Col freq	1	0.7	2.3	1.6
Cost	1	1.0	1.7	∼1.5–1.6
		Diffusivity (300 K)		
Col freq	1 (VSS)	0.7	2.2	1.5
Cost	1 (VSS)	1.0	1.6	∼1.3–1.5
		Shock wave (Ma = 4)		
Col freq	1	0.7	2.2	1.5
Cost	1	∼0.9–1.0	∼2.0–2.3	∼1.7–1.8

The location of $\bar{Q}_j$ is imposed by the x coordinate of the center of grain,

$$\bar{x}_j = x_{j+k}, \text{ for } j = 1, \ldots, \texttt{MNC} - 2k, \tag{67}$$

where x_i is the cell location of Q_i. After averaging, the cell number (i.e., the number of grains) is reduced to $\texttt{MNC} - 2k$. In this averaging scheme, adjacent grains are overlapped and their centers are a cell width apart from each other. Therefore, the distances between the nearest grains are equal to $0.1\lambda_H$ in the present work. One may give a separation between adjacent grains reducing the number of grains. Also, the averaging can be done once again using the obtained average values. There can be many different types of coarse graining. In the present work, just a simple moving average of Eq. (66) by $k = 5$ has been taken for the graining of one mean free path. For transport coefficients, the final values have been taken by averaging over seven mean free paths, taking 71 $\bar{Q}_j$'s about the center of two boundary walls,

$$\langle Q \rangle = \frac{1}{71} \sum_{j=\frac{1}{2}(\texttt{MNC}-2k)-35}^{\frac{1}{2}(\texttt{MNC}-2k)+35} \bar{Q}_j, \tag{68}$$

where $\langle Q \rangle$ is the final transport coefficient.

The grain size should be determined considering the Knudsen number. For the Couette flows, it is less than 0.1. For shock waves, the Kn number corresponds to the reciprocal shock thickness scaled by the mean free path, which amounts to 0.2–0.3 for strong shocks. The coarser graining has been carried out with $k = 5$, for one mean-free-path interval of shock profiles. It has been confirmed that there are no appreciable differences in choices, $k = 1$–5, on the shock thickness. The postprocessing of shock profiles, discussed in Sec. III B 3, should be carried out after the coarser graining.

The moving variance can be defined by

$$s_j^2 \equiv \frac{1}{2k} \sum_{i=1}^{2k+1} (Q_{j+i-1} - \bar{Q}_j)^2, \; j = 1, \ldots, \texttt{MNC} - 2k. \tag{69}$$

One may define the measure of statistical fluctuations of simulation by the formula

$$\text{fluctuation} = \sum_{j=1}^{\texttt{MNC}-2k} s_j^2. \tag{70}$$

For demonstrative purposes, we compare the fluctuations in different computations of viscosity of Ar at 300 K. The fluctuations of the xy component of the stress tensor are evaluated and shown in Fig. 7(b). As shown in the figure, the fluctuations decrease quickly at the early stage of iterations and very slowly when time steps increase and are almost indistinguishable between the single-angle computations and conventional ones.

E. Cost comparison

It is a nontrivial problem to compare the costs of DSMC for different computations. Here the cost is defined by the run time that a computer takes to produce final answers for a given condition. There may be two ways of evaluating the cost: One is by measuring the run time to reach the steady state from an initial state (called the transient method), and the other involves measuring the time it takes to produce an acceptable number of independent stationary systems, the average of which gives the final answer within a certain tolerance (called the stationary method). The latter can easily be achieved by taking an appropriate number of time steps in the simulation. However, the former essentially involves computing temporal changes and cannot be achieved by a single run but rather requires many identical computations to construct a time-dependent ensemble. The common procedure of DSMC is the stationary method. It assumes a steady state after a certain number of initial time steps and then begins sampling to construct an ensemble of systems, assuming the independence of samples. Any possible transient effects of the initial state melt away after a sufficient number of time steps. The independence of samples ensures that the average over the samples is equal to the value obtained from the transient method.

Because the independence of samples is crucial and the number of time steps required to reach the steady state is somewhat arbitrary in the stationary method, it is deemed meaningful to test and monitor the onset of the steady state before attempting to evaluate computation costs.

Let us define a running cycle as 8×10^3 time steps and test three cases of initial time steps for the steady state: 1, 10, and 100 cycles. After the initial time steps, sampling begins every eight steps. Samples are recorded at the end of every cycle. The viscosities at 300 K for three cases are computed up to 900 cycles and compared in Fig. 8(a) by the ratio to the Chapman-Enskog theoretical value. As shown in the figure, three computations show similar behaviors at the early stage of iterations. Since the initial time steps for the steady state have the role of suppressing transient effects arising from arbitrary initial states, the three cases should show different early behaviors. However, the sample size at this stage is not sufficient and the lack of independence of samples should also be considered. It seems reasonable to regard that the transient effect of initial states diminishes quickly during the first few cycles as the fluctuation does as shown in Fig. 7(a), so that the independence of samples should be more important at the early stage. The only way to have independent samples is to increase the sample size, and since all three cases have the same rate of iteration, they eventually show similar behaviors. In other computations of this work, we let the initial time steps be 100 cycles to reach a steady state, which may be more than sufficient. This test shows that ~1–10 cycles are sufficient before sampling begins

The rate of iteration can be monitored by recording the machine time taken versus the time steps. Figure 8(b) shows that the machine time is strictly proportional to the time steps. The computing cost can be defined by the slope,

$$\text{computing cost} = \frac{d(\text{machine time})}{d(\text{time step})}. \tag{71}$$

The computations for the diffusivity and shock waves give similar results. The relative computing costs for different computations are given in Table II.

The computations of this work were carried out by using the `MacMini M1` machine with the `gfortran` compiler and the `Xeon Silver4112` workstation with the `ifort` compiler.

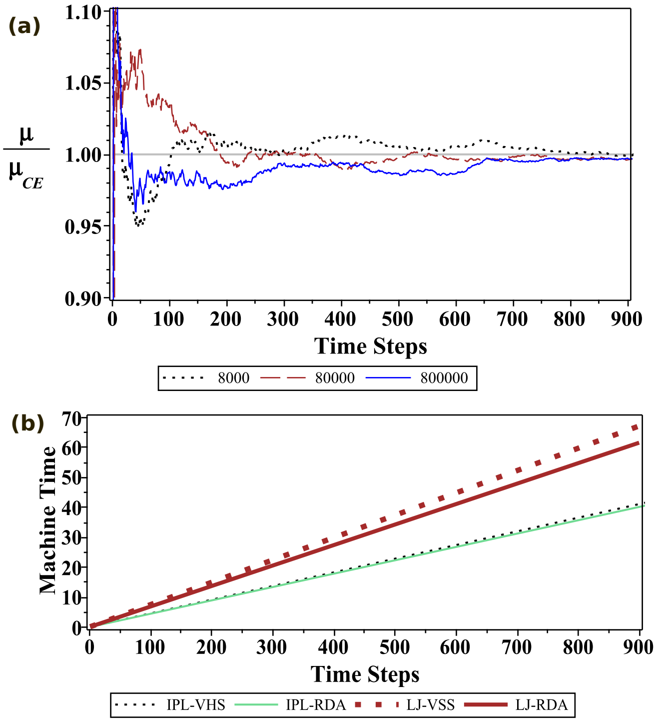

FIG. 8. (a) The IPL-RDA computations of viscosity for Ar at 300 K using different initial time steps for steady states. (b) The rate of iteration of different force models for viscosity, plotted as machine time taken versus elapsed time steps. The time steps are in increments of 8×10^3, and the machine times are in minutes using the `MacMini` machine.

IV. CONCLUSION

In the simulation of molecular systems, a proper implementation of the symmetry comprised by dynamic systems may reduce the simulation task considerably. In this respect, it is important to reveal the hidden symmetry of dynamic systems. There appears to be a hidden symmetry in the DSMC about the deflection angles. The deflection angles should in principle be given by the solution of the trajectory equation in classical mechanics (for classical problems). It is out of the question to solve the equation for every collision in the DSMC; however, the symmetry makes it possible to simulate the deflection by a preaveraged angle.

The single deflection angle simulation suggested in the present work reproduces the conventional random deflection simulations as well as the theoretical predictions by the Boltzmann equation. It is an alternative deflection algorithm for DSMC, which is applicable to any collision models. Especially, it is remarkable to have an application to the L-J force model with comparable costs to the conventional IPL models. There may be no reason that prevents the application of present suggestion to more complicated problems; however, it is certain that the suggestion should be tested in a wider range of problems, e.g., charged particles in PIC simulations [24], and 2D or 3D rarefied flows like lid-driven cavity problems [25]. Further applications of the new algorithm will be left to the DSMC community.

This paper is a revised version of the previous retracted paper [26].

APPENDIX: THE CROSS-SECTION TABLE OF L-J MOLECULES

1. Collision dynamics of L-J molecules

The relationship among χ, g, and b is given by the orbit equation, which is explained in normal textbooks of classical mechanics [8]. The equation can be applied to any intermolecular force models of physical problems. The orbit equation is well summarized in Bird's book [1], rewriting with a little different symbols,

$$\chi = \pi - 2\int_0^u \frac{dw}{\sqrt{1 - w^2 - \frac{2V}{m_r g^2}}}, \tag{A1}$$

where $w \equiv b/r$, $u \equiv b/r_m$, and r_m is the distance at the closest approach of colliding molecules; u is equal to the greatest positive root of

$$1 - u^2 - \frac{2V(b/u)}{m_r g^2} = 0. \tag{A2}$$

Let us define the dimensionless quantities,

$$\tilde{r} \equiv \frac{r}{\sigma}, \quad \tilde{g}^2 \equiv \frac{1}{2\epsilon} m_r g^2, \tag{A3}$$

which give for the L-J potential in the form

$$1 - u^2 - \frac{4}{\tilde{g}^2}\left[\left(\frac{u}{\tilde{b}}\right)^{12} - \left(\frac{u}{\tilde{b}}\right)^6\right] = 0, \tag{A4}$$

where $\tilde{b}$ is the value defined in Eq. (42). Introducing a dimensionless positive quantity ζ defined by

$$\zeta \equiv \left(\frac{u}{\tilde{b}}\right)^6 = \left(\frac{\sigma}{r_m}\right)^6, \tag{A5}$$

we rewrite Eq. (A4),

$$\tilde{g}^2(1 - u^2) + 4\zeta(1 - \zeta) = 0. \tag{A6}$$

Then the deflection angle takes the form

$$\chi = \pi - 2\int_0^u \frac{1}{\sqrt{F}} dw, \tag{A7}$$

where

$$F = 1 - w^2 + \frac{4\zeta}{\tilde{g}^2}\left(\frac{w}{u}\right)^6\left[1 - \zeta\left(\frac{w}{u}\right)^6\right]. \tag{A8}$$

The collision dynamics has two branches by the two solutions of Eq. (A6) for ζ,

$$\zeta_1 = \tfrac{1}{2}\left[1 + \sqrt{1 + \tilde{g}^2\left(1 - u_1^2\right)}\right] : \text{branch-1}, \tag{A9a}$$

$$\zeta_2 = \tfrac{1}{2}\left[1 - \sqrt{1 + \tilde{g}^2\left(1 - u_2^2\right)}\right] : \text{branch-2}, \tag{A9b}$$

with the restrictions for $\zeta > 0$,

$$0 < u_1 \leqslant u_M : \text{branch-1}, \tag{A10a}$$

$$1 < u_2 \leqslant u_M : \text{branch-2}, \tag{A10b}$$

where u_1 and u_2 are the u values of corresponding branches, and

$$u_M = \frac{1}{\tilde{g}}\sqrt{1 + \tilde{g}^2}. \tag{A11}$$

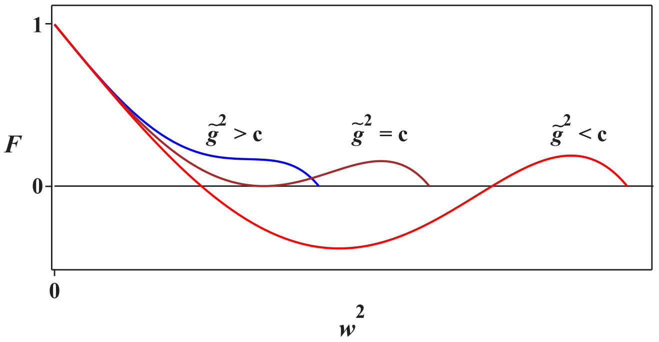

FIG. 9. Behaviors of F in Eq. (A8) for $0 \leqslant w \leqslant u_M$ when $\zeta = \frac{1}{2}$ with different $\tilde{g}^2$ values.

It is noteworthy to observe that branch-2 diappears when $\tilde{g} \to \infty$, since $u_M \to 1$ in this limit and the allowed range for u_2 in Eq. (A10b) diminishes. Then the L-J force model reduces to the IPL model. Branches 1 and 2 are considered to account for the repulsive and attractive forces, respectively.

The deflection angles are given by the integrals,

$$\chi_1 = \pi - 2\int_0^{u_1} \frac{1}{\sqrt{F_1}} dw, \tag{A12a}$$

$$\chi_2 = \pi - 2\int_0^{u_2} \frac{1}{\sqrt{F_2}} dw, \tag{A12b}$$

in which

$$F_i = 1 - w^2 + \frac{4\zeta_i}{\tilde{g}^2}\left(\frac{w}{u_i}\right)^6\left[1 - \zeta_i\left(\frac{w}{u_i}\right)^6\right], \tag{A13}$$

for $i = 1, 2$.

2. Singularity

Due to the attractive force, there is a possibility that two encountering molecules are bound and show trajectories in which the molecules circle about each other. This situation arises when $F \to 0$, giving $\chi \to -\infty$, which defines the singularity.

It seems possible to examine the singularity using graphical method. Let us first consider the case when $u_1 = u_2 = u_M$. Since $\zeta_1 = \zeta_2 = \frac{1}{2}$ in this case, the functions F_1 and F_2 take the same forms,

$$\begin{aligned} F_1 &= F_2 \\ &= 1 - w^2 + \frac{1}{\tilde{g}^2}\left(\frac{w}{u_M}\right)^6\left[2 - \left(\frac{w}{u_M}\right)^6\right], \end{aligned} \tag{A14}$$

and show the behaviors depicted in Fig. 9 for different $\tilde{g}^2$ in the ranges, $0 \leqslant w \leqslant u_M$. The singularity occurs when $\tilde{g}^2 \leqslant c$, in which c should be given by the conditions, $F = 0$, and $\partial F/\partial w = 0$. Applying these conditions to Eq. (A14), we obtain two algebraic equations for $\tilde{g}^2$ and w^2, whose simultaneous solutions are

$$\tilde{g}_c^2 \equiv c = 0.544 \cdots, \tag{A15a}$$

$$w_c^2 = 1.583 \cdots. \tag{A15b}$$

It is noteworthy to observe that there appears $F = 0$ at the point of $w = u_M$ for $\tilde{g}^2 > c$. This is not the singular point but the turning point at which the incident particle would deflect its direction giving finite χ. The integration in Eq. (A7) should be carried out up to the point of w where $F = 0$ at first.

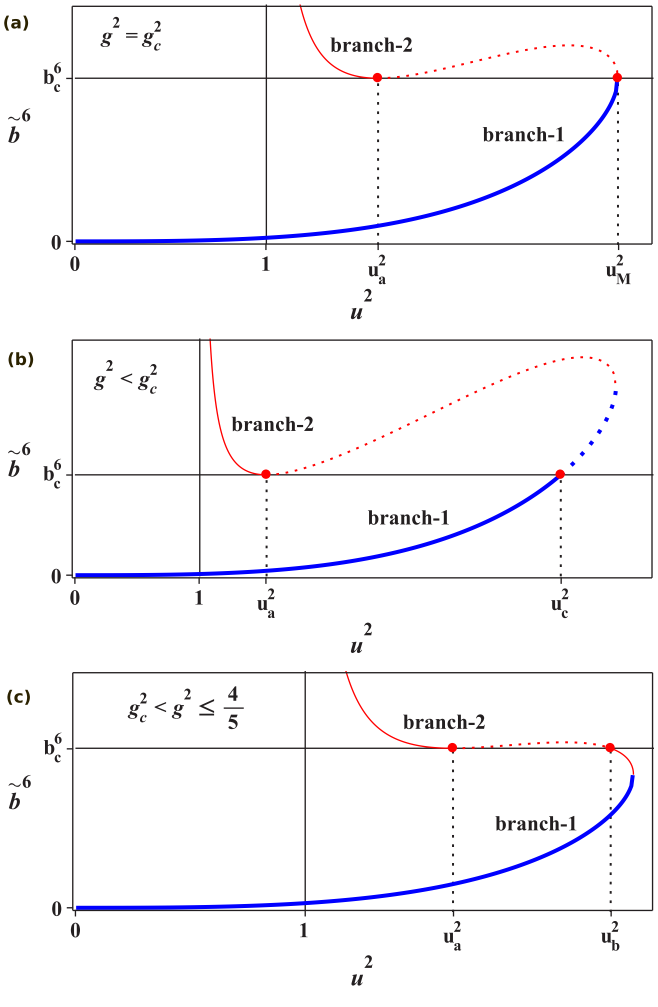

FIG. 10. Behavior of impact parameter when (a) $\tilde{g}^2 = \tilde{g}_c^2$, (b) $\tilde{g}^2 < \tilde{g}_c^2$, and (c) $\tilde{g}_c^2 < \tilde{g}^2 \leqslant \frac{4}{5}$ versus the closest approach between two colliding molecules in u, where $u = b/r_m$.

Next, consider the behavior of the impact parameter $\tilde{b}$ given in Eq. (A5). It can be written

$$\tilde{b}_i^6 = \frac{u_i^6}{\zeta_i} \tag{A16}$$

for $i = 1, 2$. Let us plot the $\tilde{b}_i^6$ at $\tilde{g}^2 = \tilde{g}_c^2$ for the allowed ranges of u_i in Eqs. (A10) as shown in Fig. 10(a). In the figure, the heavy solid curve represents branch-1, and both the thin and dotted curves are for branch-2. The dotted curve ($u_a < u_2 < u_M$) is an unphysical part of the branch-2, which gives negative F_2. Therefore, the integration of branch-2 in Eq. (A12b) gives the deflection angle only for $1 < u_2 < u_a$, while branch-1 can be integrated for the range, $0 < u_1 < u_M$. The u_a should satisfy the conditions

$$\left[\frac{\partial \tilde{b}}{\partial u}\right]_{u=u_a} = 0, \quad \left[\frac{\partial^2 \tilde{b}}{\partial u^2}\right]_{u=u_a} > 0, \tag{A17}$$

which give

$$u_a^2 = \frac{6}{25\tilde{g}^2}\left(2 + 5\tilde{g}^2 - \sqrt{4 - 5\tilde{g}^2}\right) \qquad \text{(A18)}$$

for $\tilde{g}^2 \leqslant \frac{4}{5}$.

The impact parameter at $u_2 = u_a$, writing $\widetilde{b}_c$, is obtained by

$$\widetilde{b}_c^6 = \frac{u_a^6}{\zeta_2} = \frac{432}{3125\tilde{g}^6}\,\frac{\left(2 + 5\tilde{g}^2 - \sqrt{4 - 5\tilde{g}^2}\right)^3}{5 - \sqrt{13 - 5\tilde{g}^2 + 6\sqrt{4 - 5\tilde{g}^2}}}. \qquad \text{(A19)}$$

The two small solid circles in Fig. 10(a) are the singular points at which $\chi \to -\infty$ as $F \to 0$.

a. When $\tilde{g}^2 < \tilde{g}_c^2$

In the case when $\tilde{g}^2 < \tilde{g}_c^2$, the impact parameter diagram is illustrated in Fig. 10(b). There are unphysical parts ($F < 0$) in both branch-1 and branch-2 curves, as shown by dotted curves for the ranges

$$u_c < u_1 \leqslant u_M : \text{branch-1}, \qquad \text{(A20a)}$$

$$u_a < u_2 \leqslant u_M : \text{branch-2}, \qquad \text{(A20b)}$$

in which the point u_c should be determined by the numerical solution of

$$\widetilde{b}_c^6 = \frac{u_c^6}{\zeta_1} = \frac{2u_c^6}{1 + \sqrt{1 + \tilde{g}^2\left(1 - u_c^2\right)}}, \qquad \text{(A21)}$$

within the range $u_a < u_c < u_M$. The singular points are $u_2 = u_a$ and $u_1 = u_c$, as designated by two solid circles in Fig. 10(b).

b. When $\tilde{g}_c^2 < \tilde{g}^2 \leqslant \frac{4}{5}$

It is interesting to examine the case when $\tilde{g}_c^2 < \tilde{g}^2 \leqslant \frac{4}{5}$. As shown in Fig. 10(c), there appears to be an unphysical part only in branch-2. The point at which the horizontal line cuts the branch curve, $u_2 = u_b$, should be determined numerically by solving the relation,

$$\widetilde{b}_c^6 = \frac{u_b^6}{\zeta_2} = \frac{2u_b^6}{1 - \sqrt{1 + \tilde{g}^2\left(1 - u_b^2\right)}}, \qquad \text{(A22)}$$

within the range $u_a < u_b < u_M$. It should be carefully noted that $F_2 > 0$ when $u_b < u_2 \leqslant u_M$ giving regularity. The $u_2 = u_a$ and u_b are the singular points giving $\chi \to -\infty$, which are designated by solid circles in Fig. 10(c).

c. When $\tilde{g}^2 > \frac{4}{5}$

When $\tilde{g}^2 = \frac{4}{5}$, two singular points of branch-2 coincide at $u_a^2 = u_b^2 = \frac{9}{5}$, and when $\tilde{g}^2 > \frac{4}{5}$, there is no singularity for all the allowed ranges of u_1 and u_2 [Eqs. (A10)], as noted by Hirschfelder in 1948 [27].

3. Deflection angles

It is straightforward to obtain the χ's in Eqs. (A12) by numerical integration, excluding the unphysical singular ranges.

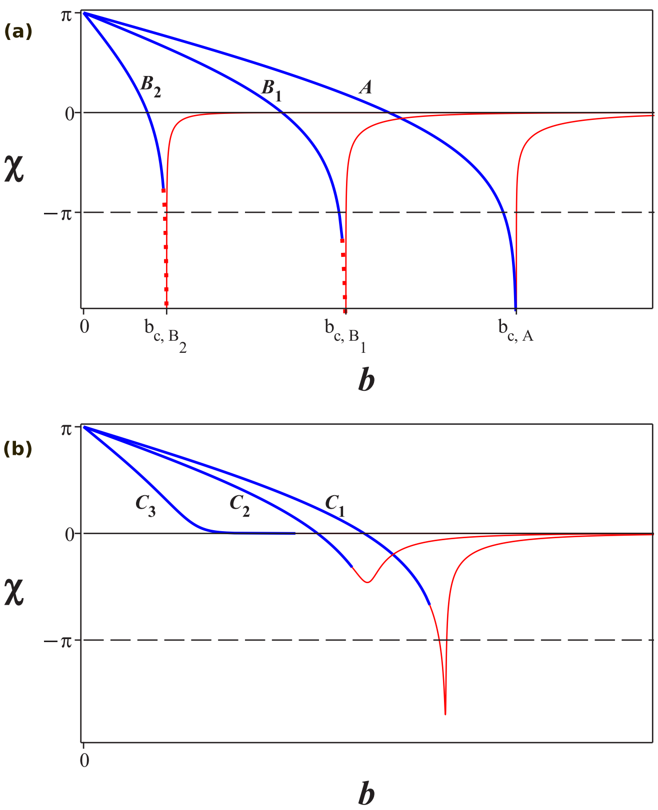

FIG. 11. Deflection angles and their singularities versus impact parameters. Upper curves in (a): A for $\tilde{g}^2 \leqslant \tilde{g}_c^2$; B_1 and B_2 for $\tilde{g}_c^2 < \tilde{g}^2 \leqslant \frac{4}{5}$. Lower curves in (b): C_1 for $\tilde{g}^2 \gtrsim \frac{4}{5}$; C_2 for a typical behavior in the region of $\tilde{g}^2 > \frac{4}{5}$; C_3 for $\tilde{g}^2 \to \infty$.

a. Deflection angles when $\tilde{g}^2 \leqslant \tilde{g}_c^2$

In this case, both branches-1 and -2 have singularity. For the integration, $0 < w < u_i$, the upper limit should be

$$0 < u_1 < u_c : \text{branch-1}, \qquad \text{(A23a)}$$

$$1 < u_2 < u_a : \text{branch-2}, \qquad \text{(A23b)}$$

where u_a is in Eq. (A18) and u_c is given by the numerical solution of Eq. (A21). The behavior of χ is depicted in Fig. 11(a) by curve A. The critical impact parameter is designated by $b_{c,A}$ in the figure.

b. Deflection angles when $\tilde{g}_c^2 < \tilde{g}^2 \leqslant \frac{4}{5}$

Branch-1 has no singular point in this case but branch-2 has two. The integration limit, u_2, should be carefully considered for branch-2. First, we integrate with the limits,

$$0 < u_1 \leqslant u_M : \text{branch-1}, \qquad \text{(A24a)}$$

$$1 < u_2 < u_a : \text{branch-2}, \qquad \text{(A24b)}$$

as shown by the solid lines of curves $B_1(\tilde{g}^2 < 0.67)$ and $B_2(\tilde{g}^2 > 0.68)$ in Fig. 11(a). We need additional integration for branch-2 to the limit

$$u_b < u_2 \leqslant u_M : \text{branch-2}, \qquad \text{(A25)}$$

which is shown by the dotted lines. The u_b is given by the numerical solution of Eq. (A22). The critical impact parameters of this case are designated by b_{c,B_1} and b_{c,B_2} in Fig. 11(a).

c. Deflection angles when $\widetilde{g}^2 > \frac{4}{5}$

In this is the case, where both branches are regular, the integration limits are

$$0 < u_1 \leqslant u_M : \text{branch-1}, \qquad \text{(A26a)}$$

$$1 < u_2 \leqslant u_M : \text{branch-2}. \qquad \text{(A26b)}$$

The results of numerical integration are depicted in Fig. 11(b). Curve C_1 in the figure represents the values for $\frac{4}{5} < \widetilde{g}^2 < 1.01$, and curve C_2 represents the value for $\widetilde{g}^2 > 1.01$, showing a typical behavior in this region. Curve C_3 represents the behavior of χ when $\widetilde{g}^2 \to \infty$, in which the branch-2 disappears.

4. Cross-section table

It is straightforward to obtain $\widetilde{\Sigma}_D$ and $\widetilde{\Sigma}_\mu$ by numerically integrating Eqs. (41) using the values of χ and $\widetilde{b}$ obtained. Because the singularity of deflection angles does not give rise to a physical discontinuity, it has been conventional to assume a functional form of χ around the singular point and integrate analytically [27,28],

$$\chi^2 = \frac{\text{constant}}{\widetilde{b}^2 - \widetilde{b}_c^2}. \qquad \text{(A27)}$$

In order for the contributions of the analytical integrals to the cross section to be less than a few percentages, the integration limit of $\widetilde{b}$ should be sufficiently close to $\widetilde{b}_c$. Results are tabulated in the Supplemental Material [17].

At the limit when $\widetilde{g}^2 \to \infty$, it is possible to have a limiting law for the cross sections. Since the upper limit of the integration in Eqs. (A26), $u_M \to 1$, as seen in Eq. (A11), branch-2 does not contribute to the deflections and the integration limit of branch-1 becomes

$$0 < u_1 \leqslant 1 : \text{branch-1}. \qquad \text{(A28)}$$

Considering the limiting value in Eq. (A9a),

$$\zeta_1 \to \tfrac{1}{2}\sqrt{\widetilde{g}^2\left(1 - u_1^2\right)}, \qquad \text{(A29)}$$

we see from Eq. (A13),

$$F_1 \to 1 - w^2 - \left(1 - u_1^2\right)\left(\frac{w}{u_1}\right)^{12}, \qquad \text{(A30)}$$

which is equal to the equation for χ of IPL molecules,

$$V = 4\epsilon\left(\frac{\sigma}{r}\right)^{12}. \qquad \text{(A31)}$$

The cross sections at $\widetilde{g}^2 \to \infty$ have the values

$$\Sigma_D \to 2\pi\sigma^2(\widetilde{g}^2)^{-\frac{1}{6}}(0.6590), \qquad \text{(A32a)}$$

$$\Sigma_\mu \to 2\pi\sigma^2(\widetilde{g}^2)^{-\frac{1}{6}}(0.5313), \qquad \text{(A32b)}$$

which give

$$\langle\Sigma\rangle = 2\pi\sigma^2(\widetilde{g}^2)^{-\frac{1}{6}}(0.5520), \qquad \text{(A32c)}$$

$$\cos\langle\chi\rangle = -0.1938. \qquad \text{(A32d)}$$

At the limit when $\widetilde{g}^2 \to 0$, both branches 1 and 2 survive. However, we can examine the $\widetilde{g}^2$-dependence of the cross section by examining the behavior of $\widetilde{b}_c$ in Eq. (A19). Since

$$\lim_{\widetilde{g}\to 0} \widetilde{b}_c^6 = \frac{27}{\widetilde{g}^2}, \qquad \text{(A33)}$$

it is certain that $\widetilde{b}^2 \sim (\widetilde{g}^2)^{-1/3}$, which reveals the limiting property of cross sections at $\widetilde{g}^2 \to 0$. By extrapolating the numerical values obtained, we have the limiting laws,

$$\Sigma_D \to 2\pi\sigma^2\left(\widetilde{g}^2\right)^{-\frac{1}{3}}(1.243), \qquad \text{(A34a)}$$

$$\Sigma_\mu \to 2\pi\sigma^2(\widetilde{g}^2)^{-\frac{1}{3}}(0.9410), \qquad \text{(A34b)}$$

which give

$$\langle\Sigma\rangle = 2\pi\sigma^2(\widetilde{g}^2)^{-\frac{1}{3}}(1.00), \qquad \text{(A34c)}$$

$$\cos\langle\chi\rangle = -0.243. \qquad \text{(A34d)}$$

[1] G. A. Bird, *Molecular Gas Dynamics and the Direct Simulation of Gas Flows* (Clarendon Press, New York, 1994).

[2] G. A. Bird, *The DSMC Method, Version 1.2* (CreateSpace Independent Publishing Platform, San Bernardino, CA, 2013).

[3] G. A. Bird, M. A. Gallis, J. R. Torczynski, and D. J. Rader, Accuracy and efficiency of the sophisticated direct simulation monte carlo algorithm for simulating noncontinuum gas flows, Phys. Fluids **21**, 017103 (2009).

[4] M. A. Gallis and J. R. Torczynski, Normal solutions of the Boltzmann equation for highly nonequilibrium Fourier flow and Couette flow, Int. J. Numer. Methods Fluids **67**, 1057 (2011).

[5] A. Venkattraman, A. A. Alexeenko, M. A. Gallis, and M. S. Ivanov, A comparative study of no-time-counter and majorant collision frequency numerical schemes in DSMC, AIP Conf. Proc. **1501**, 489 (2012).

[6] E. Roohi and S. Stefanov, Collision partner selection schemes in DSMC: From micro/nano flows to hypersonic flows, Phys. Rep. **656**, 1 (2016).

[7] S. K. Stefanov, On the basic concepts of the direct simulation Monte Carlo method, Phys. Fluids **31**, 067104 (2019).

[8] H. Goldstein, J. L. Safko, and J. C. P. Poole, *Classical Mechanics*, 3rd ed. (Pearson Education Ltd., London, 2014).

[9] D. V. Widder, *Advanced Calculus*, 2nd ed. (Dover, New York, 1989).

[10] N. Alves and J. Stark, The direct simulation Monte Carlo of flows composed of asymmetric potential scatters, Phys. Fluids **14**, 1403 (2002).

[11] G. A. Bird, Comment on “Direct simulation Monte Carlo method for an arbitrary intermolecular potential” [Phys. Fluids 24, 011703 (2012)], Phys. Fluids **25**, 049101 (2013).

[12] K. Koura and H. Matsumoto, Variable soft sphere molecular model for Inverse-Power-Law or Lennard-Jones potential, Phys. Fluids A **3**, 2459 (1991).

[13] A. Venkattraman and A. A. Alexeenko, Binary scattering model for Lennard-Jones potential: Transport coefficients and

collision integrals for non-equilibrium gas flow simulations, Phys. Fluids **24**, 027101 (2012).

[14] A. B. Weaver, A. Venkattraman, and A. A. Alexeenko, Binary scattering model for Lennard-Jones potential: Transport coefficients and collision integrals for non-equilibrium gas flow simulations, Phys. Fluids **26**, 107102 (2014).

[15] A. B. Weaver and A. A. Alexeenko, Revised variable soft sphere and Lennard-Jones model parameters for eight common gases up to 2200K, J. Phys. Chem. Ref. Data **44**, 023103 (2015).

[16] F. Sharipov, Direct simulation Monte Carlo method based on *abinitio* potential: Recovery of transport coefficients of multicomponent mixtures ofnoble gases, Phys. Fluid **34**, 097114 (2022).

[17] See Supplemental Material at http://link.aps.org/supplemental/10.1103/PhysRevE.108.035301 for the cross section table of 210 rows and 5 colums.

[18] S. Chapman and T. G. Cowling, *The Mathematical Theory of Non-Uniform Gases*, 3rd ed. (Cambridge University Press, London, 1970).

[19] J. O. Hirschfelder, C. F. Curtiss, and R. B. Bird, *Molecular Theory of Gases and Liquids* (Wiley, New York, 1964).

[20] K. Koura and H. Matsumoto, Variable soft sphere molecular model for air species, Phys. Fluids A **4**, 1083 (1992).

[21] J. Kestin, K. Knierim, E. A. Mason, B. Najafi, S. T. Ro, and M. Waldman, Equilibrium and transport properties of the noble gases and their mixtures at low density, J. Phys. Chem. Ref. Data **13**, 229 (1984).

[22] E. Vogel, B. Jager, R. Hellmann, and E. Bich, *Ab initio* pair potential energy curve for the argon atom pair and thermophysical properties for the dilute argon gas. II. Thermophysical properties for low-density argon, Mol. Phys. **108**, 3335 (2010).

[23] H. Alsmeyer, Density profiles in argon and nitrogen shock waves measured by the absorption of an electron beam, J. Fluid Mech. **74**, 497 (1976).

[24] V. Vahedi and M. Surendra, A Monte Carlo collision model for the particle-in-cell method: Application to argon and oxygen discharges, Comput. Phys. Commun. **87**, 179 (1995).

[25] Z. Mengbo, E. Roohi, and A. Ebrahimi, Computational study of rarefied gas flow and heat transfer in lid-driven cylindrical cavities, Phys. Fluids **35**, 052012 (2023).

[26] Y. G. Ohr, Retraction: Mean scattering angle method for direct simulation Monte Carlo [Phys. Rev. E **105**, 015302 (2022)], Phys. Rev. E **107**, 019902(E) (2023).

[27] J. O. Hirschfelder, R. B. Bird, and E. L. Spotz, The transport properties for nonpolar gases, J. Chem. Phys. **16**, 968 (1948).

[28] E. Mason, Transport properties of gases obeying a modified Buckingham (Exp-Six) potential, J. Chem. Phys. **22**, 169 (1954).